JOURNAL OF PROPULSION AND POWER
Vol. 21, No. 1, January–February 2005

Comparison of Simulated Magnetoplasmadynamic Thruster Flowfields to Experimental Measurements

K. Sankaran,* E. Y. Choueiri,† and S. C. Jardin‡
Princeton University, Princeton, New Jersey 08544

The flowfield of a magnetoplasmadynamic thruster was simulated numerically using an advanced code specifically developed for this purpose, and the results were compared to experimental measurements, to validate the code and obtain insight into underlying physical processes. The thruster chosen was the full-scale benchmark thruster because it has been the subject of many experimental studies. The parallelized axisymmetric code featured detailed physical models and a finite volume formulation that allowed for nonorthogonal grids. Flowfield properties, such as electron density, velocity, current density, electron temperature, ionization fraction, and mass and momentum flux, as well as thrust, compared favorably with existing data. The simulation provided insight into some aspects of thruster operation, such as the weak role of the anode geometry in affecting the thrust, the predominantly electromagnetic nature of the thrust at nominal operating conditions, and the importance of the near-cathode region in energy dissipation. The simulated structure of the flow was found to embody a number of photographically recorded features of the actual discharge.

Nomenclature

$\boldsymbol{B}$ = magnetic induction
$\bar{\mathcal{B}}_M$ = Maxwell stress tensor
E = electric field strength
E' = electric field seen by the plasma
$\mathcal{E}$ = energy density of the plasma
e = charge of an electron
h = Planck's constant
g = statistical weight of an energy level
J = current
$\boldsymbol{j}$ = current per unit area
k = coefficient thermal conduction
k_B = Boltzmann's constant
m = mass of a particle
n = number density of a species
p = pressure
Q = collision cross section; partition function
$\boldsymbol{q}$ = energy flux
T = temperature; thrust
$\boldsymbol{u}$ = fluid velocity
Z = effective ionization level $n_e \Big/ \sum n_i$
ϵ = electronic energy level
ϵ_0 = permittivity of free space
η = resistivity
μ_0 = permeability of free space
ν = collision frequency
ξ = dimensionless current
ρ = mass density

Subscripts

EM = electromagnetic
e = electrons
ex = exhaust
h = heavy species, Ar I, Ar II, Ar III, Ar IV
i = ions
w = wall
ψ = stream function, $r B_\theta$

Presented as Paper 2003-4843 at the AIAA/ASME/SAE/ASEE 39th Joint Propulsion Conference, Huntsville, AL, 20–23 July 2003; received 20 September 2003; revision received 22 April 2004; accepted for publication 18 April 2004.

*Ph.D. Candidate, Mechanical and Aerospace Engineering Department.
†Chief Scientist, Electric Propulsion and Plasma Dynamics Laboratory and Associate Professor, MAE Department. Associate Fellow of AIAA.
‡Principal Research Scientist, Princeton Plasma Physics Laboratory and Professor, Astrophysical Sciences Department.

I. Introduction

THE Princeton full-scale benchmark thruster (FSBT) is a magnetoplasmadynamic thruster (MPDT) that has been the subject of many experimental investigations[1–9] over the past three decades. Yet, there has not been a detailed numerical simulation of this device. Now, with the improvements in numerical methods[10,11] and computing capability,[12] it is worthwhile to revisit this device, by comparing experimental measurements to results from a recently developed code.[12] Another goal of this comparison is to validate this code for future use with thrusters for which experimental data are not yet widely available, such as the lithium Lorentz force accelerator (LiLFA).[13]

The underlying numerical schemes of this code are based on the principles of conservation formulation, characteristics splitting, and flux-limited antidiffusion to solve the governing equations. This code was introduced by the authors in Ref. 14 and is described in detail in Ref. 10. This code also contains models for various classical and anomalous transport phenomena and a real equation of state, for a realistic description of the MPDT plasma. The use of this code to simulate the flowfield in a constant-area channel MPDT[15] is described in Ref. 10.

In Sec. II, we describe the governing equations and the physical models used in this simulation. Then, in Sec. III, we describe how these equations were formulated to be solved in a nonorthogonal coordinate system in a conservative fashion. In Sec. IV, we discuss the discretization method and the boundary conditions imposed on the solver to calculate the flowfield in self-field MPDT. In Sec. V, we present the results from the simulation of plasma flows in the FSBT and compare the results to experimental measurements. In Sec. VI, we use these aforementioned results to investigate some underlying physical processes in the FSBT.

II. Physical Model

The governing equations for a MHD flow problem are the conservation relations for mass, momentum, magnetic flux, and energy.

The conservation relations for mass density, momentum density, magnetic flux, and energy density can be written in the form (cf., Ref. 10)

$$\frac{\partial}{\partial t}\begin{bmatrix}\rho\\ \rho\boldsymbol{u}\\ \boldsymbol{B}\\ \mathcal{E}\end{bmatrix}+\nabla\cdot\begin{bmatrix}\rho\boldsymbol{u}\\ \rho\boldsymbol{u}\boldsymbol{u}+\bar{\bar{\mathrm{p}}}-\bar{\bar{\mathcal{B}}}_M\\ \boldsymbol{u}\boldsymbol{B}-\boldsymbol{B}\boldsymbol{u}\\ (\mathcal{E}+p)\boldsymbol{u}-\bar{\bar{\mathcal{B}}}_M\cdot\boldsymbol{u}\end{bmatrix}=\boldsymbol{D} \tag{1}$$

The right-hand side (RHS) of Eq. (1), $\boldsymbol{D}$, contains the dissipative effects that are physical in nature, and they, too, are written as divergence of fluxes, as seen in Appendix A.

In the momentum equation, $\bar{\bar{\mathcal{B}}}_M=(1/\mu_0)[\,\boldsymbol{B}\boldsymbol{B}-(B^2/2)\boldsymbol{I}\,]$ is the magnetic part of the Maxwell stress tensor, and it satisfies the relation

$$\nabla\cdot\bar{\bar{\mathcal{B}}}_M=\boldsymbol{j}\times\boldsymbol{B} \tag{2}$$

In Faraday's law, the contribution of back emf to the change in magnetic field is written as a divergence of a flux,

$$-\nabla\times(\boldsymbol{u}\times\boldsymbol{B})=\nabla\cdot(\boldsymbol{u}\boldsymbol{B}-\boldsymbol{B}\boldsymbol{u}) \tag{3}$$

The energy equation is written in terms of the energy density (energy per unit volume) $\mathcal{E}$, which includes the internal energy, kinetic energy, and the energy in the magnetic field. The dissipative flux of energy, $\nabla\cdot\boldsymbol{q}$, contains the ohmic heating (written in terms of divergence of the Poynting flux) and thermal conduction,

$$\nabla\cdot\boldsymbol{q}=\nabla\cdot[(\boldsymbol{B}\times\boldsymbol{E}')/\mu_0+\bar{\bar{k}}\cdot\nabla T]$$

In addition to the total energy equation, we needed to account for the disparity between electron and ion temperatures. The conservation relations for the internal energy density of electrons $\mathcal{E}_e$ can be written as

$$\frac{\partial\mathcal{E}_e}{\partial t}+\nabla\cdot[\mathcal{E}_e\boldsymbol{u}]+p_e\nabla\cdot\boldsymbol{u}=\eta j^2-\Delta\dot{\mathcal{E}}_{ie}+\nabla\cdot(k_e\nabla T_e) \tag{4}$$

In expression (4), ηj^2 is the ohmic heating term. The rate of exchange of energy per unit volume between the electrons and the ions, through collisions $\Delta\dot{\mathcal{E}}_{ie}$ is

$$\Delta\dot{\mathcal{E}}_{ie}=\frac{3\rho_e\nu_{ei}}{M_i}k_B(T_e-T_i) \tag{5}$$

where ρ_e is the electron mass density and ν_{ei} is the average collision frequency between electrons and ions.

The internal energy of ions can be obtained by subtracting electron internal energy from the total internal energy.

A. Transport Phenomena

The transport phenomena included in our model are electron and ion thermal conduction, classical electrical resistivity with Hall effect, and anomalous transport (see Ref. 16).

Our method for the calculation of classical transport coefficients relies on momentum transfer during elastic collisions. The energy-weighted average of the momentum transfer collision frequency between the electrons and species s is given by (cf., Refs. 17 and 18)

$$\nu_{es}=n_s Q_{es}\sqrt{8k_BT_e/\pi m_e} \tag{6}$$

If the species in consideration is an ion of charge q, then

$$Q_{eq}=\frac{\pi}{4}\left(\frac{Z_q e^2}{4\pi\epsilon_0 k_B T_e}\right)^2\ell_n\left[1+\frac{144\pi^2(\epsilon_0 k_B T_e)^3}{n_e e^6 Z^2(Z+1)}\right] \tag{7}$$

The electron–neutral collision cross section for argon is $Q_{e0}\simeq 4.0\times 10^{-20}$ m^2, and the ion–neutral collision cross section is $Q_{i0}\simeq 1.4\times 10^{-18}$ m^2. The ion–ion collision frequency is estimated by[17]

$$Q_{ii}=\left[(5.845\times 10^{-10})/T_h^2\right]\ell_n 1.239\times 10^7\sqrt{T_h^3/n_e} \tag{8}$$

From the mentioned relations for collision frequencies, the coefficient for the electron thermal conductivity can be estimated as

$$k_e=3.20\frac{k_B^2 n_e T_e}{m_e\sum_s\nu_{es}} \tag{9}$$

whereas that of the ions is

$$k_i=\sqrt{\frac{\pi k_B^3 T_h}{8M_i}}\left(\frac{n_i}{n_i Q_{ii}+n_0 Q_{i0}}\right) \tag{10}$$

The electrical resistivity is defined as

$$\eta_0\equiv\frac{m_e\sum_s\nu_{es}}{n_e e^2} \tag{11}$$

and the electron Hall parameter is

$$\Omega_e=\frac{\omega_{c,e}}{\sum_s\nu_{es}}=\frac{eB/m_e}{\sum_s\nu_{es}} \tag{12}$$

The anomalous transport model takes into account the enhanced transport due to momentum exchange between particles in the plasma and waves induced by current-driven microinstabilities in a collisional and finite-β magnetized plasma.[19] As a result, the effective resistivity of the plasma can be expressed as

$$\eta_{\mathrm{eff}}=\frac{m_e\left(\nu_{e_{\mathrm{cl}}}+\nu_{e_{\mathrm{an}}}\right)}{e^2 n_e} \tag{13}$$

Details for calculating $\nu_{e_{\mathrm{an}}}$ are given in Ref. 16, and Ref. 12, the details of how they are incorporated into this code are given.

B. Equation of State

For argon, the ideal gas model is not accurate for temperatures greater than 0.5 eV. The relationship between pressure and temperature is nonlinear and has to be computed using the relation

$$p=nk_BT\frac{\partial\,\ell_n Q}{\partial V} \tag{14}$$

and is shown in Fig. 1. The partition function Q was obtained from Ref. 20. Because energy is deposited into internal modes, the ratio of specific heats deviates significantly from the ideal value of $\frac{5}{3}$. In our model, the ratio of specific heats, shown in Fig. 2, was computed from the partition function obtained from Ref. 2.

C. Ionization

The plasma in a self-field, quasi-steady MPDT is generally in a state of ionizational nonequilibrium.[21] Although some numerical simulations (such as in Ref. 22) have used finite-rate ionization

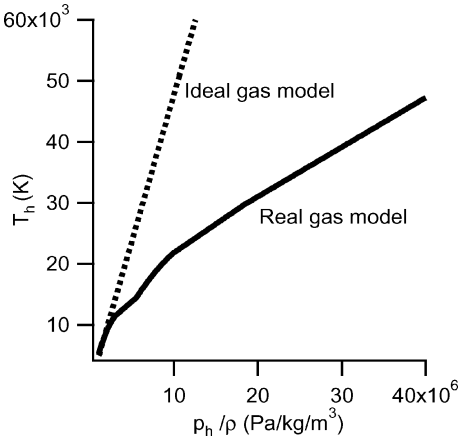

Fig. 1 Deviation from ideal-gas behavior for argon (calculated from data in Ref. 20).

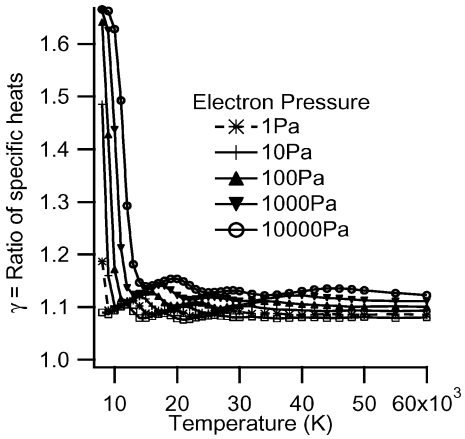

Fig. 2 Variation of the ratio of specific heats for argon (calculated from data in Ref. 20).

models, they do not include higher levels of ionization that have been observed experimentally.[23,24] In the present work, as in Refs. 25 and 26, we use a multilevel equilibrium ionization model, where the densities of electrons, n_e, ions, n_i, and neutrals, n_0, are related by the Saha equation,

$$\frac{n_i n_e}{n_{i-1}} = \frac{2(2\pi m_e k_B T_e)^{\frac{3}{2}}}{h^3} \frac{\sum_l g_l^i \exp\left(-\epsilon_l^i / k_B T_e\right)}{\sum_l g_l^{i-1} \exp\left(-\epsilon_l^{i-1} / k_B T_e\right)} \tag{15}$$

in which ϵ_l^i is the lth energy level of the species of ionization level i, and g_l^i is the corresponding statistical weight. The relevant energy levels of argon atom and its ions, and their statistical weights were obtained from Refs. 27 and 28.

III. Finite Volume Formulation

Equation (1) describes conservation relations for mass density, momentum density, magnetic flux, and energy density. However, in reality, the conserved quantities are mass, momentum, magnetic flux, and energy. Therefore, the first, second, and the fourth equations in the set Eq. (1) need to be multiplied by the volume of the cell.

Equations of the form

$$\frac{\partial U}{\partial t} = \frac{\partial f}{\partial r} + \frac{\partial g}{\partial z} + S \tag{16}$$

on multiplication by the cell volume $(2\pi r\, \mathrm{d}r\, \mathrm{d}z)$ take the form

$$\frac{\partial (rU)}{\partial t} = \frac{\partial (rf)}{\partial r} + \frac{\partial (rg)}{\partial z} + (S - f) \tag{17}$$

The expanded form of these equations is given in Appendix A.

Equations such as Eq. (17) can be written in their integral form. Every one of these conservation laws (for mass, radial momentum, axial momentum, magnetic flux, and total energy) can be individually written as

$$\iint_A \left[\frac{\partial U}{\partial t} = \left(\frac{\partial Fr}{\partial r} + \frac{\partial Fz}{\partial z} \right) + \text{source} \right] \mathrm{d}A \tag{18}$$

The first term on the RHS can be expressed as the curl of a vector $\hat{\boldsymbol{F}} = [Fz, -Fr]$ because

$$\nabla \times \hat{\boldsymbol{F}}|_\theta = \frac{\partial \hat{F}_r}{\partial z} - \frac{\partial \hat{F}_z}{\partial r} = \frac{\partial Fr}{\partial r} + \frac{\partial Fz}{\partial z} \tag{19}$$

Using the Stokes theorem, this curl over the cell area can be expressed as the line integral around the edges of the cell,

$$\iint_A \frac{\partial U}{\partial t}\, \mathrm{d}A = \oint \hat{\boldsymbol{F}} \cdot \mathrm{d}l + \iint_A (\text{source})\, \mathrm{d}A \tag{20}$$

Because this equation is true irrespective of the shape of the control volume, the fluxes Fr and Fz, can be written in the (r, z) coordinate system, as in Appendix A, regardless of the shape of the cell. This is a fundamental advantage of the finite volume formulation over the finite difference formulation, in addition to maintaining conservation.

IV. Numerical Solution

The techniques for the numerical solution of Eqs. (1–4) are described in Ref. 10, and in this section we will only discuss how they are used to obtain solution for the flowfield in a self-field MPDT.

A. Spatial Discretization

Mathematically, the governing equations (1–4) are mixed hyperbolic and parabolic partial differential equations. The discretization scheme for the hyperbolic (convective) part of the problem involves using the characteristics to estimate fluxes through the cell surfaces and is described in Ref. 10.

Unlike convective fluxes, dissipative fluxes depend on gradients, and we need to compute derivatives across the surfaces for estimating j_r, j_z, $\partial T/\partial r$, and $\partial T/\partial z$. In an orthogonal grid system, we can estimate gradients by simply differencing the values in adjacent cells. However, in a nonorthogonal grid, the adjacent cells/points are not along the lines of constant r or z. Therefore, here we have to estimate gradients in a different manner. This involves using the Stokes theorem, and this method is described in Appendix B.

B. Boundary Conditions

In this section, we will discuss the estimation of the convective and dissipative terms at various boundaries.

1. *Flow Properties*

Freestream. The computational domain is taken to be large enough (four anode radii downstream of anode tip) so that there are no normal gradients in any of the flow properties at the freestream boundaries.

Solid walls. The governing equations require the value of thermal conduction between the wall and the plasma to be specified. This can either be given explicitly (as in the case of adiabatic walls, such as the insulated inner side of the chamber, where the thermal conduction is zero), or can be computed by fixing the temperature of the wall. In this simulation, the wall temperature is set to 2500 K at metallic boundaries, consistent with experimental data (cf., Ref. 29), as well as other simulations (cf., Ref. 26).

Centerline. At the axis of symmetry, there are no radial convective fluxes. Moreover, there are no radial gradients. Therefore, there is no thermal conduction across the centerline.

Inlet. At the inlet, a specified mass flow rate of the propellant enters at a specified temperature at sonic conditions. In reality, the propellant is injected as neutral gas at room temperature, and it gets almost fully ionized within a few millimeters from the inlet.[24] Classical theory cannot explain this high rate of ionization, and it has been proposed[30] that a non-Maxwellian electron energy distribution, resulting from plasma microturbulence, is the cause for this. Because this process cannot be modeled by fluid theory, the inlet temperature in our simulation is chosen to be high enough (1.0 eV) such that the propellant is sufficiently ionized. Effectively, the backplate of the numerical model is not the true backplate, but a region located few millimeters downstream of it.

On this issue, our simulation distinctly differs from that of Refs. 26 and 31. In both these simulations, the propellant is injected at close to room temperatures, and ionization is allowed to develop in a classical fashion. Therefore, in both Refs. 26 and 31, the plasma is only weakly ionized through most of the thruster channel. However, experimental measurements[24,32] show that the propellant is

fully ionized upstream in the channel. Therefore, in our simulation, the plasma is set to be fully ionized at the inlet.

2. Field Properties

Freestream. The computational domain is chosen to be large enough such that all of the current is enclosed within the domain. Thus, from Ampère's law, the magnetic field at the freestream boundaries is zero.

Solid walls. At all other boundaries, the magnetic field is computed from Faraday's law, which through Stokes theorem can be written as

$$\int_A \frac{\partial \boldsymbol{B}}{\partial t} \cdot \mathrm{d}\boldsymbol{A} = -\oint_C \boldsymbol{E} \cdot \mathrm{d}\boldsymbol{l} \tag{21}$$

In the cell-centered scheme used in this work, Eq. (21) implies that the evolution of the magnetic flux is specified by the contour integral of the electric field around a cell. Therefore, the only information required is the electric field drop along the boundaries. Because of the no mass flux condition, the electric field is entirely resistive and is given by

$$\boldsymbol{E}_w = \eta_w \boldsymbol{j}_w \tag{22}$$

The surface current $\boldsymbol{j}_w$ is computed from Ampère's law in the usual manner. At conducting boundaries, all of the current entering the discharge flows at the surface, at least in the transient case. Therefore, even though resistivity η_w for most conductors is very small (e.g., $\eta_w = 5.6 \times 10^{-8}\ \Omega \cdot \mathrm{m}$ for tungsten) compared to the plasma resistivity [typically, $\mathcal{O}(10^{-3} - 10^{-4})\ \Omega \cdot \mathrm{m}$], the surface electric field is significant, due to the large current density in the transient case. In a true steady state, after the magnetic field has diffused into the conductor, the surface potential drop decreases to zero.

At insulated boundaries, the magnetic field diffuses into the wall instantaneously. Therefore, the jump in the magnetic field, and subsequently the surface current, is zero.

Centerline. As a result of symmetry, the inductive component of the electric field is zero because there is no flow across it. However, the resistive component is finite. This can be obtained from the value of the magnetic field at a point close to $r = 0$, through a simple Taylor series expansion (see Ref. 33),

$$E_z|_{r=0} = E_z'|_{r=0} = \eta j_z|_{r=0} = \eta \frac{4B_\theta|_{\Delta r/2}}{\mu_0 \Delta r} \tag{23}$$

Inlet. Because all of the enclosed current is downstream of the inlet (the backplate shown in Fig. 3), the stream function $\psi = rB_\theta = \mu_0 J_{\mathrm{tot}}/2\pi$ is a constant at any given time, inasmuch as it depends only on the total current. The electric field along the backplate, required for Faraday's law, is then

$$E_r(r, 0) = E_r(r, \Delta z) + \Delta z \left(\frac{1}{r} \frac{\partial \psi}{\partial t} - \frac{\partial E_z}{\partial r} \right) \tag{24}$$

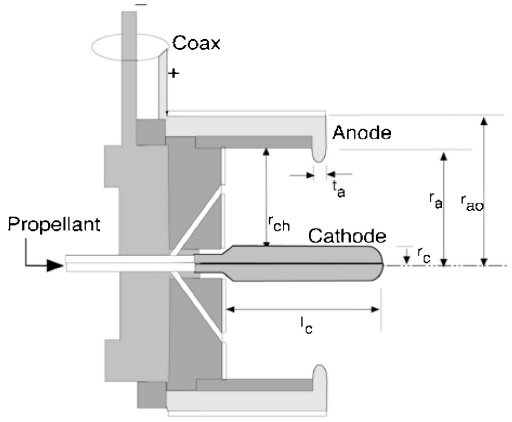

Fig. 3 Princeton FSBT, where $r_c = 0.95$, $r_a = 5.1$, $r_{a0} = 10.2$, $r_{ch} = 6.4$, $t_a = 0.95$, and $l_c = 10.0$ cm.

Insulator. Similarly, all of the current is also downstream of the insulator on the inner wall of the chamber (Fig. 3) where the electric field is

$$E_z(R_{ch}, z) = E_z(R_{ch} - \Delta r, z) + \Delta r \left(\frac{1}{r} \frac{\partial \psi}{\partial t} + \frac{\partial E_r}{\partial z} \right) \tag{25}$$

V. MPDT Simulation Results

The geometry chosen for this simulation was the Princeton FSBT.[9] It was chosen because of extensive experimental work that has been done on it.[1–9] The relevant dimensions are given in Fig. 3. In this paper, we only consider a propellant mass flow rate of 6.0 g/s of argon and vary the current from 12.0 to 20.0 kA (Table 1).

The dimensionless current ξ represents the discharge current normalized by the critical ionization current J_{ci} at which an equipartition of energy (or power) between the acceleration and ionization sinks is reached. At that condition, we can write

$$\dot{m} u_{\mathrm{ex}}^2 \big/ 2 = T^2/2\dot{m} = \dot{m}\epsilon_i / M \tag{26}$$

which, along with the Maecker thrust law (see Ref. 34) $T = bJ^2$, where

$$b = (\mu_0/4\pi)[\ell_n (r_a/r_c)] \tag{27}$$

is a geometrical constant, leads to the definition

$$\xi = J/J_{\mathrm{ci}} = (u_{\mathrm{ci}}/b)^{\frac{1}{2}} \tag{28}$$

where $u_{\mathrm{ci}} \equiv \sqrt{(2\epsilon_i/M)}$ is the so-called critical ionization velocity. A number of experimental studies[35] have shown that many aspects of MPDT performance and operation scale with ξ (or ξ^2) irrespective of power level.

The case with a total current of 16.0 kA (at $\dot{m} = 6.0$ g/s) corresponds to the nominal operating condition of $\xi \simeq 1.0$ (Ref. 35) and, therefore, will be of special interest to us.

For simplicity, the rounded corners of the anode lip and the cathode were truncated in the simulation. Note that in the simulation the thruster contains four mass injection ports: One at the base of the cathode (as in Fig. 3) at a 45-deg angle, and three others at $r = 2$, 3, and 4 cm through the backplate directed normally into the chamber. In reality, several mass injections schemes were tested in experimental studies, and the version shown in Fig. 3 has only one port through the backplate.

The code described in this paper solves the governing equations in a time-dependent manner. Therefore, to verify convergence, we monitored the time-dependent change; see Eq. (1). The criterion we used was $\Delta t(\nabla \cdot F) \leq 10^{-7}$ (Fig. 4), and it was reached roughly at 300 μs. The sudden change around $t = 50\ \mu$s is because we changed the $\mathrm{d}J/\mathrm{d}t$ value at that point.

We now present some of the results of the simulation. A summary of some of them are presented in Table 1. In Table 1, the first column contains the current level (in kiloamphere), the second the

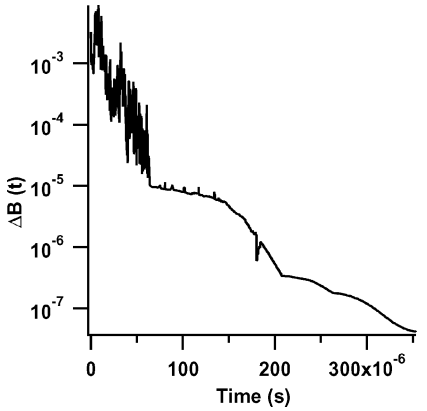

Fig. 4 Convergence history: change in magnetic field vs time.

Table 1 FSBT simulation summary

Current, kA	ξ	T_{calc}, N	T_{exp}, N	T_{EM}/T_{tot}, %	V_{plasma}, V	P_{in}, kW
12.0	0.82	33.3	30.8	60	28.0	336.0
16.0	1.09	51.2	50.4	75	36.0	576.0
17.5	1.19	59.3	61.5	78	49.4	864.5
20.0	1.36	77.0	82.7	80	62.4	1248.0

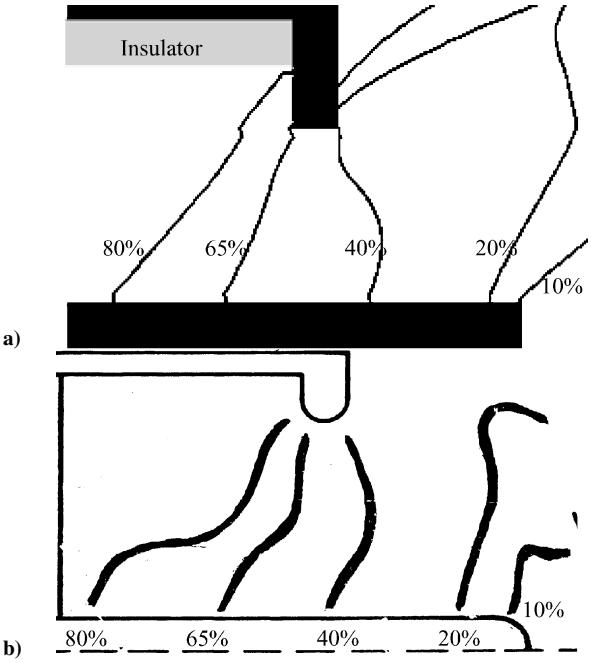

Fig. 5 Current contours for $J = 20.0$ kA and $\dot{m} = 6.0$ g/s: a) calculated and b) measured (obtained from Ref. 36).

corresponding nondimensional value of the current, the third the calculated value of thrust (in newton), the fourth the measured value of thrust (in newton), the fifth the calculated ratio of electromagnetic thrust to total thrust. The sixth column contains the calculated values of voltage drop in the plasma (in volt), and the seventh contains the calculated value of power input to the plasma (in kilowatt).

A. Current

The calculated contours of enclosed current are shown in Fig. 5, in comparison with experimental measurements.[36] For the sake of brevity, we only show the comparison at the most challenging of the operating conditions listed in Table 1 ($J = 20$ kA). As evident from Fig. 5, the simulation predicts the attachment locations of the 80, 60, and the 40% contours accurately on both the cathode and the anode. For the 20 and the 10% lines, the attachment on the cathode is also predicted accurately. In the front face of the anode (in the plume), however, we are unable to make a comparison because of the lack of data at that location. In any case, the continuum assumption [inherent in Eq. (1)] would limit the validity of the simulations in the low collisionality region of the plume.

B. Thrust and Voltage

By definition, the thrust is computed using the following relation:

$$T = \int_A u_z(\rho \boldsymbol{u} \cdot \mathrm{d}\boldsymbol{A}) \tag{29}$$

The calculated values of thrust are compared to measurements,[9] and the results are presented in Table 1. At the lowest current (12.0 kA, $\xi = 0.82$), the code overpredicts thrust by 8%, and at the highest current (20.0 kA, $\xi = 1.36$), the code underpredicts by 7%. At the nominal operating condition (16.0 kA, $\xi = 1.09$), the agreement is within 2%.

The plasma voltage drop is presented for various current levels in Table 1. For the nominal operating condition ($J = 16.0$ kA, $\dot{m} = 6.0$ g/s), this simulation predicts a plasma voltage drop of 36 V, as shown in Fig. 6. Note that the simulation did not include electrode fall voltages, and therefore, we cannot compare the calculated plasma voltage to the measured total voltage[9] directly. Measurements[8] have shown repeatedly that the anode fall can be $\simeq$50 V at $\xi \simeq 1.0$, and this is a major energy sink in an MPDT. Note that the monotonic increase of voltage with current is consistent with measurements.[9]

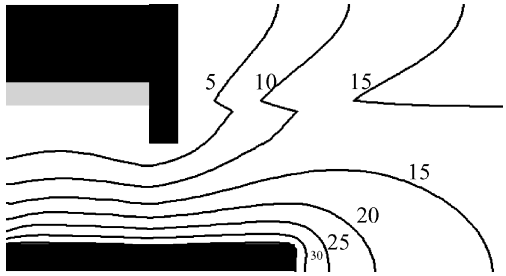

Fig. 6 Calculated potential contours (in volts).

C. Density

The electron number density contours within the chamber are shown in Fig. 7a, for the $\xi = 1.09$ case. Note that, inside the chamber, n_e increases toward the cathode. This is attributed to the action of the radial pumping force, $j_z B_\theta$, which pushes the plasma toward the cathode. This trend has been observed in experiments and in previous simulations.[22] The density in the thruster chamber ranges from $\simeq 2.0 \times 10^{20}\mathrm{m}^{-3}$ near the chamber wall to $\simeq 5.0 \times 10^{21}$ m^{-3} near the cathode. Outside the chamber, on the centerline near the cathode, one also finds a region of high density ($\simeq 5.0 \times 10^{21}$ m^{-3}), which is often termed the cathode jet.[37] In this simulation, the highest density, $\simeq 2.0 \times 10^{22}$ m^{-3}, is found near the injection port on the base of the cathode. Although there exist no detailed measurements of electron density in the FSBT, Turchi and Jahn[37] measured them for a similar geometry (dubbed as configuration A) with a shorter cathode. As reported in Ref. 37, electron number densities near the cathode in the chamber and on the centerline in front of the cathode are, indeed, around $\simeq 5.0 \times 10^{21}$ m^{-3} and are in accordance with the results of the simulation.

It is well known from experimental measurements[7,8] that the anode region of the FSBT gets starved of charge carriers as the current is increased. Our simulations show this trend clearly. In Figs. 7e–7g, we show the calculated values of electron number density (per cubic meter) near the anode for $J = 12.0$ kA (panel e), $J = 16.0$ kA (panel f), and $J = 20.0$ kA (panel g). This starvation could play an important role in understanding the performance-limiting onset of instabilities in the FSBT.[7,8]

D. Velocities

The contours of axial velocity are shown in Fig. 7b. The range of values (8.0–13.0 km/s) is in the range of measured values of local velocities reported in Ref. 38 for these conditions. On the centerline, Boyle[39] measured axial velocity increasing from 10 to 13 km/s, with distance from 2 to 15 cm in front of the cathode. It can be seen in Fig. 8 that this simulation also predicts a similar pattern and values.

E. Temperature

The calculated values of electron temperature are shown in Fig. 7c, for the $\xi = 1.09$ case. In the bulk of the chamber, T_e ranges from 1.0 to 1.75 eV, which is in the range of measurements in Ref. 40. The rear top end of the chamber has lowest values (0.75 eV) because it has the lowest ohmic-heating rate. The highest values of $\simeq$3.5 eV are found on the inner and outer faces of the anode. This can be explained by the large ohmic heating caused by the high-current density observed in that region. Diamant[8] measured temperatures around 2.5 eV near the anode at this condition, and they are in general agreement with the simulation, in that region. Temperatures of $\simeq$3.0 eV are seen in the simulation in front of the cathode on the centerline.

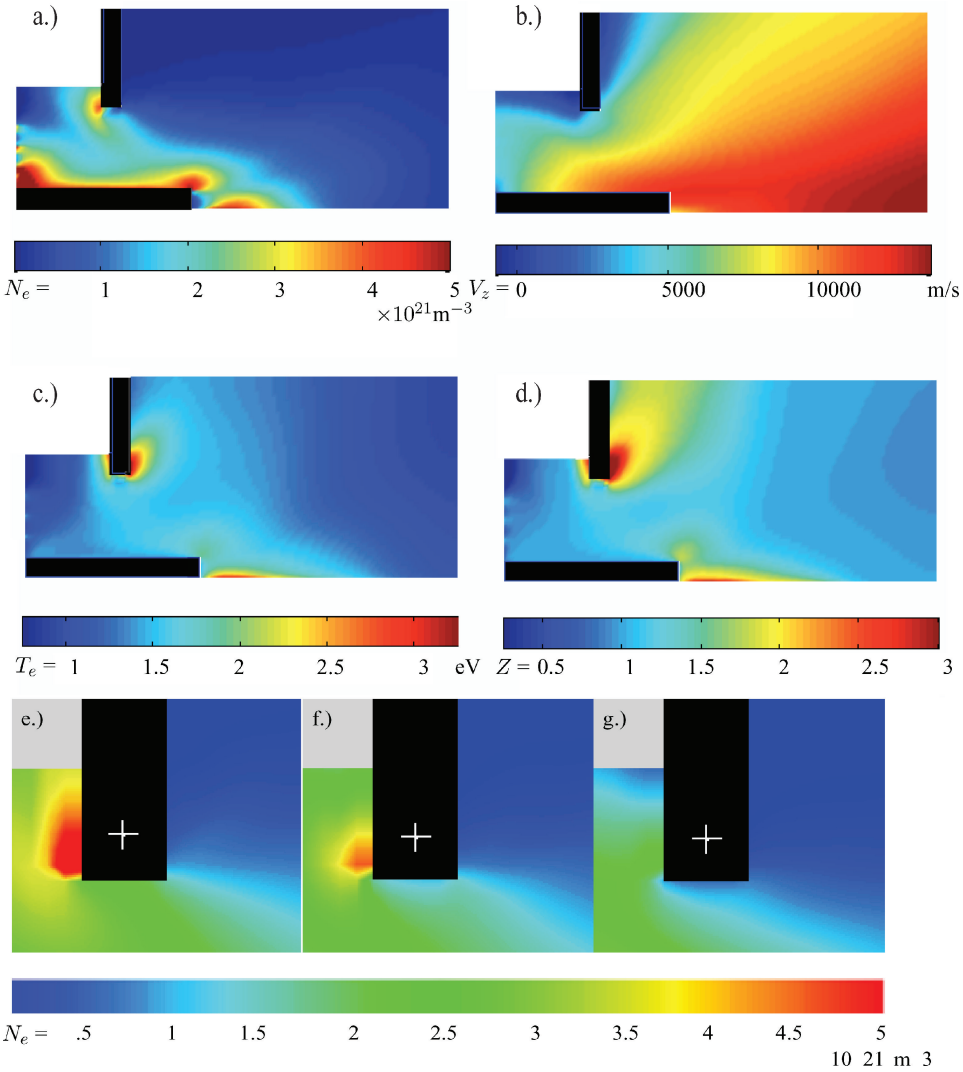

Fig. 7 Electrons, $\dot{m} = 6.0$ g/s and $J = 16.0$ kA: a) calculated electron number density (per cubic meter), b) calculated axial velocity (meters per second), c) calculated electron temperature (electron volts), and d) calculated effective ionization fraction and electron number density near anode starving with increasing current: e) ($J = 12.0$ kA, f) $J = 16.0$ kA, and g) $J = 20.0$ kA.

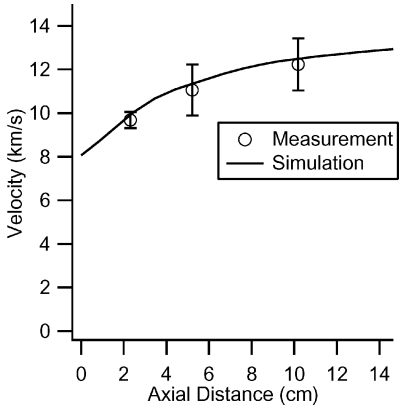

Fig. 8 Comparison of measured[39] and calculated centerline velocities at $J = 16.0$ kA, $\dot{m} = 6.0$ g/s.

For the $\xi = 1.36$ case ($J = 20$ kA), the near-anode temperatures reach 4.5–5.0 eV. Measurements by Diamant[8] have shown that this is indeed the case.

VI. Insight into MPDT Physical Processes

As evident from the preceding section, this simulation has predicted many of the salient features of the flowfield, and the results are in general agreement with measurements for many quantities.

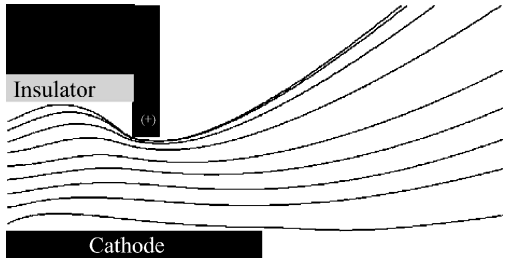

Fig. 9 Calculated velocity streamlines at $J = 16.0$ kA, $\dot{m} = 6.0$ g/s.

Therefore, we can now use this simulation to delve into some of the physical mechanisms of the MPDT. Unless explicitly stated otherwise, we will focus on the operation at $J = 16.0$ kA (at $=6.0$ g/s) because this corresponds to the nominal operating condition of $\xi \simeq 1.0$.

A. Effect of the Anode Lip

The velocity streamlines in the FSBT are shown in Fig. 9. The expansion of the streamlines past the anode lip, and hence plume divergence, is evident from Fig. 9. It is clear that the anode lip is an obstruction to the streamlines, and its stagnation effect can be seen in the increased density (Fig. 7a) and temperature (Fig. 7c) in that region.

To ascertain the effect of the anode lip on thrust, we need to look at the mass flux and the momentum flux in this thruster.

J. S. Cory[41] measured the mass flux at this operating condition for the configuration A thruster (which has a similar geometry to the FSBT, but with a shorter conical cathode). The results of this simulation are compared to those measurements in Fig. 10. Generally, the agreement between the simulation and the data is very good. Except for the point on the centerline, the agreement is within 20%. Near the centerline, the measured mass flux is higher than that predicted by the simulation. This may be attributed to the difference in the cathode lengths in the experiment and the simulation.

As seen in Fig. 10, the flux of mass near the anode is relatively small. More important, as seen in Fig. 11, the flux of momentum in the anode region is small compared to the cathode region. Because of a combination of the pumping force ($j_z B_\theta$) pushing the plasma toward the cathode and the $1/r^2$ variation of the axial Lorentz force

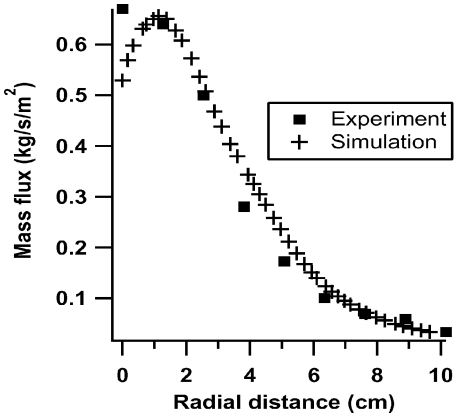

Fig. 10 J.S. Mass flux at a distance of 12.5 cm from the anode plane; no error bars on the measurements were provided in the original work.[41]

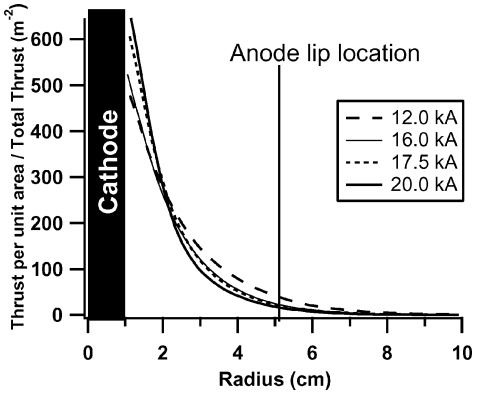

Fig. 11 Calculated momentum flux at the cathode tip plane.

density ($j_r B_\theta$), the high-speed jet is confined to the cathode region of the thruster, and the anode region does not play a significant role in the momentum flux. Furthermore, the results shown in Fig. 11 clearly indicate that the contribution of the anode region in the thrust production decreases with increasing $J^2/\dot{m}$. Therefore, the anode lip is not a significant impediment to the production of thrust at these operating conditions.

B. Ionization Levels

The effective ionization fraction is shown in Fig. 7d. Note that this simulation uses an equilibrium ionization model, and hence, $Z = Z(n, T_e)$. Therefore, an understanding of T_e distribution is important to understand the distribution of ionization levels. In the rear top end of the chamber, where the current density is low ($\simeq 5.0 \times 10^4$ A/m^2), we find that the ionization level is low ($Z \simeq 0.25$), as expected. In the bulk of the chamber, $Z \simeq 1.0$. Near the inner face of the anode and the anode lip, where the current density is high, the effective ionization level ranges from 1.5 to 2.5. In the outer edge of the anode, current density is also very high, the ionization level is $\simeq$3.0. The presence of these higher states of ionization (Ar III and Ar IV) has been shown by Bruckner[23] in the anode plane of the configuration A thruster, for these operating conditions (argon at 6.0 g/s, $J = 16.0$ kA).

C. Discharge Structure

In many experimental observations[1,42] at nominal operating conditions, the luminous structure of the discharge was observed to have some invariant features, such as a cathode jet, a luminous barrel that is larger at the base of the cathode and constricts toward the middle and expands again at the cathode tip. All of these features can be seen in Fig. 12. In Fig. 12a are the calculated values of electron density, whereas Fig. 12b shows the observed argon ion emission from the discharge recorded photographically using an FSBT with transparent walls.[42] The similarity in the calculated and observed structure of the discharge is evident. This is the first instance, to our knowledge, where numerical simulations of such thruster flows are compared directly to visual observations.

D. Current on the Cathode

The current distribution on the cathode is shown in Fig. 13. Near the inlet, the surface current density has a value of $\simeq$550 A/cm^2 and quickly decreases to $\simeq$200 A/cm^2 along most of the cathode, only to rise again near its tip. In Fig. 13, this is compared with the measurements by Boyle,[39] who measured similar values along the cathode. However, whereas Boyle reports that the current density at the cathode tip is in excess of 1000 A/cm^2, the simulation only predicts $\simeq$550 A/cm^2. This difference could be because the cathode in Ref. 39 was shorter than that of the FSBT and had a conical tip, as opposed to the hemispherical tip of the FSBT. As seen in Fig. 13, the longer cathode (simulation) has a greater surface area and, hence,

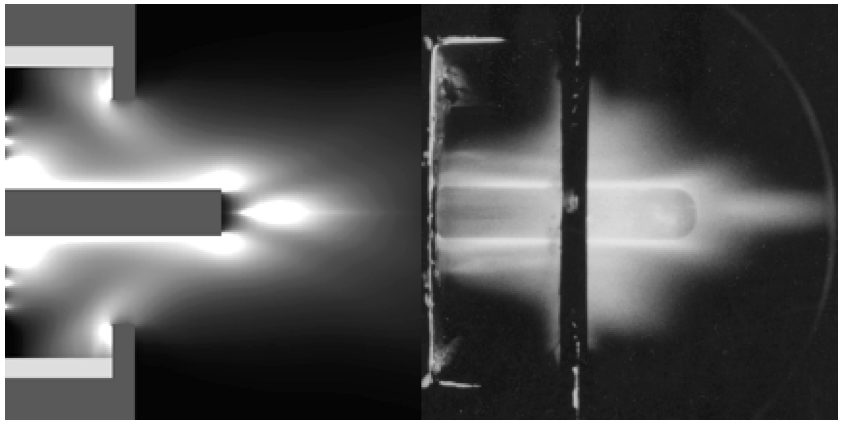

a) b)

Fig. 12 Discharge structure, $J = 16.0$ kA and $\dot{m} = 6.0$ g/s: a) calculated electron number density and b) observed argon ion emission from the discharge recorded photographically using an FSBT with transparent walls.[42]

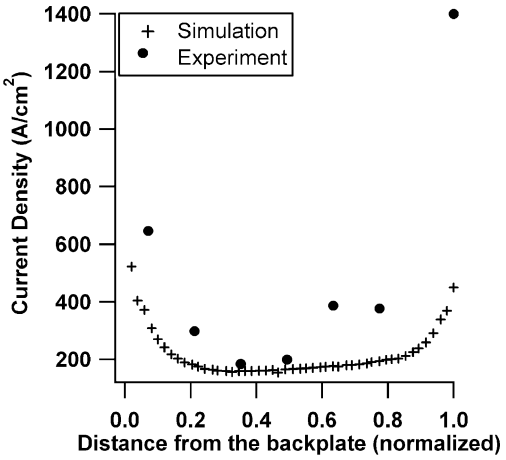

Fig. 13 Surface current density on the cathode; error bars on the measurement not available in the original source.[39]

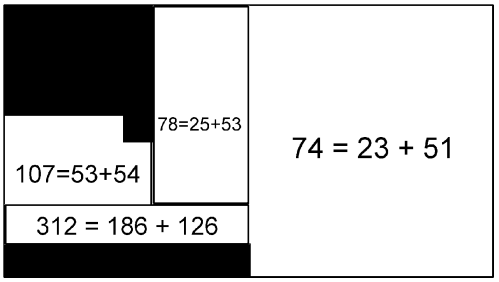

Fig. 14 Power expenditure (in kilowatt) in various regions; read as total power = kinetic power + ohmic heating.

lesser current density. This may play a role in reducing erosion, as well as in decreasing ohmic dissipation (to be discussed).

E. Thrust Composition

The electromagnetic contribution to the thrust T_{EM} is

$$T_{\mathrm{EM}} = \int (\boldsymbol{j} \times \boldsymbol{B})\, \mathrm{d}V \tag{30}$$

The fractional contribution of the electromagnetic thrust to the total thrust is presented in Table 1. The other component, namely, the electrothermal, is substantial when $\xi < 1.0$. (For instance, at $\xi = 0.82$, 40% of thrust is electrothermal.) However, the importance of electrothermal thrust decreases, and the importance of electromagnetic thrust increases, with increasing current. From Table 1, it is clear that at $\xi \geq 1.0$ (which for argon is $J = 16.0$ kA for 6.0 g/s), the FSBT is predominantly an electromagnetic accelerator.

F. Energy Deposition

The total power deposited into the MPDT plasma can be split into kinetic power and dissipation,

$$\int \boldsymbol{j} \cdot \boldsymbol{E}\, \mathrm{d}V = \int (\boldsymbol{j} \times \boldsymbol{B}) \cdot \boldsymbol{u}\, \mathrm{d}V + \int \eta j^2\, \mathrm{d}V \tag{31}$$

The second term on the RHS is often termed the "dissipation integral,"[15] and understanding and quantifying it are essential to improving the efficiency of the MPDT. We have calculated all of the three terms in Eq. (31) for the FSBT, and the results are shown in Fig. 14. Note that these calculations do not include the power dissipated in the electrode fall, which can be a significant loss mechanism.

In a coaxial configuration, the current density is inversely proportional to the radius, and therefore, the power deposition and the dissipation are large near the cathode. This is evident in Fig. 14, where almost 45% of the dissipation occurs in the inner flow region,[39] which is restricted to 1 cm around the cathode. As with thrust production (discussed in Sec. VI.A), this near cathode region is an important one in energetics as well. For consistency, one can verify that the sum of all of the input power in all of the zones in Fig. 14 add up to VJ (571 kW) (Table 1).

Note that the shell near the cathode is the only region where the kinetic power exceeds the ohmic heating (which is largely unrecovered because of the lack of a nozzle or other mechanism to convert it into thrust).

VII. Conclusions

We have described the reformulation of our MHD code that was developed for the simulation of propulsive plasma flows. We presented the physical models: the two-temperature MHD equations with suitable transport properties, ionization, and equation of state models. We also discussed the techniques for obtaining a numerical solution of the governing equations.

The code was used to simulate plasma flows in the Princeton FSBT. The calculated contours of density, ionization levels, velocity, mass flux patterns, enclosed current contours, cathode surface current density, and temperature compared well with measurements at similar operating conditions. The calculated value of thrust matched with the measured value within 2% at the nominal operating condition.

The code was then used to provide insight into some physical mechanisms. Among the important observations are the following three.

1) Despite being a cause of stagnation in a part of the flow, the anode lip does not have a serious adverse effect on the thrust.

2) The FSBT is predominantly an electromagnetic accelerator at its nominal operating condition ($J = 16$ kA for $\dot{m} = 6.0$ g/s of argon).

3) The inner-flow region, 1 cm around the cathode, plays an important role in the energetics.

Currently, this code is being utilized to simulate the operation of the FSBT at other regimes of operation. The next goal of this effort is to simulate the performance of other thrusters, such as the LiLFA, for which there is a dearth of data.

Appendix A: Governing Equations

The finite volume formulation of Eq. (1) is

$$\frac{\partial}{\partial t}\begin{bmatrix} r\rho \\ r\rho u \\ r\rho w \\ B_\theta \\ r\mathcal{E} \end{bmatrix} = \frac{\partial}{\partial r}\begin{bmatrix} -r\rho u \\ -r\left(\rho u^2 + p + \dfrac{B^2}{2\mu_0}\right) \\ -r\rho u w \\ E'_z - uB_\theta \\ -r\left(u\left(\mathcal{E} + p + \dfrac{B^2}{2\mu_0}\right) - q_r\right) \end{bmatrix} + \frac{\partial}{\partial z}\begin{bmatrix} -r\rho w \\ -r\rho u w \\ -r\left(\rho w^2 + p + \dfrac{B^2}{2\mu_0}\right) \\ -(E'_r + wB_\theta) \\ -r\left(w\left(\mathcal{E} + p + \dfrac{B^2}{2\mu_0}\right) - q_z\right) \end{bmatrix} + \begin{bmatrix} 0 \\ p - \dfrac{B^2}{(2\mu_0)} \\ 0 \\ 0 \\ 0 \end{bmatrix} \tag{A1}$$

Appendix B: Derivatives in Nonorthogonal Coordinates

Recall that if some vector $\hat{\boldsymbol{B}} = [0, -rB]$, then

$$\nabla \times \hat{\boldsymbol{B}} = \frac{\partial (rB)}{\partial r} \tag{B1}$$

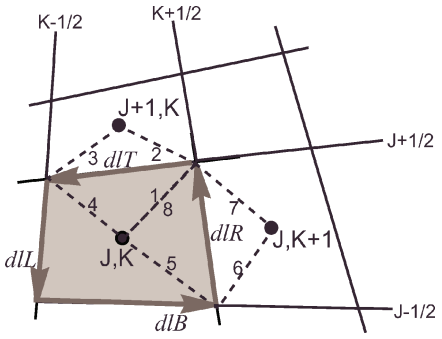

Fig. B1 General nonorthogonal control volume.

Using Stokes theorem, this becomes

$$j_z = \frac{1}{\mu_0}\frac{1}{r}\frac{\partial(rB)}{\partial r} = \frac{1}{\mu_0}\frac{1}{r}\frac{1}{A\left[J+\frac{1}{2}\right][K]}\oint [0, -rB]\cdot \mathrm{d}\boldsymbol{l} \quad \text{(B2)}$$

Similarly, if $\hat{\boldsymbol{B}} = [B, 0]$, then

$$\nabla \times \hat{\boldsymbol{B}} = \frac{\partial B}{\partial z} \quad \text{(B3)}$$

which becomes,

$$j_r = -\frac{1}{\mu_0}\frac{\partial B}{\partial z} = -\frac{1}{\mu_0}\frac{1}{A[J]\left[K+\frac{1}{2}\right]}\oint [B,\ 0]\cdot \mathrm{d}\boldsymbol{l} \quad \text{(B4)}$$

Here, $A[J][K+\frac{1}{2}]$ and $A[J+\frac{1}{2}][K]$ refer to the areas of the dotted cells in Fig. B1 to the right and top, respectively. They can be estimated a simple averages of the control volumes.

The contour integrals in Eqs. (B2) and (B4) require estimation of B along $\mathrm{d}\boldsymbol{l}$, which is the dotted line in Fig. B1. First, the line element vectors $\mathrm{d}\boldsymbol{l}$ have to be computed from the coordinates of the vertices and the center of the cell. Then, B along this line element can be obtained by averaging from the nearby cell centers.

References

[1]Rudolph, L. K., "The MPD Thruster Onset Current Performance Limitation," Ph.D. Dissertation, Mechanical and Aerospace Engineering Dept., Princeton Univ., Princeton, NJ, 1980.

[2]Ho, D. D., "Erosion Studies in a (MPD) Thruster," M.S. Thesis, Mechanical and Aerospace Engineering Dept., Princeton Univ., Princeton, NJ, 1981.

[3]Kaplan, D. I., "Performance Chatacteristics of Geometrically-Scaled Magnetoplasmadynamic (MPD) Thrusters," M.S. Thesis, Mechanical and Aerospace Engineering Dept., Princeton Univ., Princeton, NJ, 1982.

[4]Wolff, M. J., "A High Performance Magnetoplasmadynamic Thruster," M.S. Thesis, Mechanical and Aerospace Engineering Dept., Princeton Univ., Princeton, NJ, 1984.

[5]Gilland, J. H., "The Effect of Geometric Scale upon MPD Thruster Behavior," M.S. Thesis, Mechanical and Aerospace Engineering Dept., Princeton Univ., Princeton, NJ, 1988.

[6]Hoskins, W. A., "Asymmetric Discharge Patterns in the MPD Thruster," M.S. Thesis, Mechanical and Aerospace Engineering Dept., Princeton Univ., Princeton, NJ, 1990.

[7]Gallimore, A. D., "Anode Power Deposition in Coaxial MPD Thrusters," Ph.D. Dissertation, Mechanical and Aerospace Engineering Dept., Princeton Univ., Princeton, NJ, 1992.

[8]Diamant, K. D., "The Anode Fall in a High Power Pulsed MPD Thruster," Ph.D. Dissertation, Mechanical and Aerospace Engineering Dept., Princeton Univ, Princeton, NJ, 1996.

[9]Choueiri, E. Y., and Ziemer, J. K., "Quasi-Steady Magnetoplasmadynamic Thruster Performance Database," *Journal of Propulsion and Power*, Vol. 17, 2001, pp. 967–976.

[10]Sankaran, K., Martinelli, L., Jardin, S. C., and Choueiri, E. Y., "A Flux-Limited Numerical Method for the MHD Equations to Simulate Propulsive Plasma Flows," *International Journal of Numerical Methods in Engineering*, Vol. 53, No. 5, 2002, pp. 1415–1432.

[11]Sankaran, K., Choueiri, E. Y., and Jardin, S. C., "Application of a New Numerical Solver to the Simulation of MPD Flows," AIAA Paper 2000-3537, 2000.

[12]Sankaran, K., Jardin, S. C., and Choueiri, E. Y., "Parallelization and Validation of an MHD Code for the Simulation of Self-Field MPDT Flows," *Proceedings of the 27th International Electric Propulsion Conference*, Paper IEPC-01-127, 2001.

[13]Ageyev, V. P., and Ostrovsky, V. G., "High-Current Stationary Plasma Accelerator of High Power," *Proceedings of the 23rd International Electric Propulsion Conference*, Paper IEPC-93-117, 1993.

[14]Sankaran, K., and Choueiri, E. Y., "An Accurate Characteristics-Splitting Scheme for Numerical Solution of MHD Equations," *Proceedings of the 26th International Electric Propulsion Conference*, Paper IEPC-99-208, 1999.

[15]Villani, D. D., "Energy Loss Mechanisms in a Magnetoplasmadynamic Arcjet," Ph.D. Dissertation, Mechanical and Aerospace Engineering Dept., Princeton Univ., Princeton, NJ, 1982.

[16]Choueiri, E. Y., "Anomalous Resistivity and Heating in Current-Driven Plasma Thrusters," *Physics of Plasmas*, Vol. 6, No. 5, 1999, p. 2290.

[17]Mitchner, M., and Kruger, C. H., *Partially Ionized Gases*, Willy-Interscience, New York, 1973.

[18]Heiermann, J., Auweter-Kurtz, M., and Sleziona, P. C., "Adaptive Computation of the Current-Carrying Plasma in an MPD Rocket Thruster," *Time-Dependent Magnetohydrodynamics: Anayltical, Numerical, and Application Aspects*, 1998.

[19]Choueiri, E. Y., "Instability of a Current-Carrying Finite-Beta Collisional Plasma," *Physical Review E*, Vol. 64, No. 6, 2001.

[20]Sparks, W. M., and Fischel, D., "Partition Functions and Equations of State in Plasmas," NASA SP-3066, 1971.

[21]Sheppard, E. J., "Ionization Nonequilibrium and Ignition in Self-Field Magnetoplasmadynamic Thrusters," Ph.D. Dissertation, Aeronautics and Astronautics Dept., Massachusetts Inst. of Technology, Cambridge, MA, 1992.

[22]Niewood, E. H., "An Explanation for Anode Voltage Drops in an MPD," Ph.D. Dissertation, Aeronautics and Astronautics Dept., Massachusetts Inst. of Technology, Cambridge, MA, 1993.

[23]Bruckner, A. P., "Spectroscopic Studies of the Exhaust Plume of a Quasi-Steady MPD Accelerator," Ph.D. Dissertation, Mechanical and Aerospace Engineering Dept., Princeton Univ., Princeton, NJ, 1972.

[24]Randolph, T. M., "Measurement of Ionization Levels in the Interelectrode Region of an MPD Thruster," M.S. Thesis, Mechanical and Aerospace Engineering Dept., Princeton Univ., Princeton, NJ, 1994.

[25]Schrade, H. O., Sleziona, P. C., Wegmann, T., and Kurtz, H. L., "Basic Processes of Plasma Propulsion: Final Report," U.S. Air Force Office of Scientific Research Rept. AFOSR 91-0118, 1991.

[26]LaPointe, M. R., and Mikellides, P. G., "High Power MPD Thruster Development at the NASA Glenn Research Center," AIAA Paper 01-3499, 2001.

[27]Vlcek, J., "A Collisional-Radiative Model Applicable to Argon Discharges over A Wide Range of Conditions: Formulation and Basic Data," *Journal of Physics D Applied Physics*, Vol. 22, No. 5, 1989, pp. 623–631.

[28]Kaufmann, V., and Whaling, W., "Improved Wavelengths and Energy Levels of Doubly-Ionized Argon (Ar III)," *Journal of Research of the National Institute of Standards and Technology*, Vol. 101, No. 5, 1996, pp. 691–704.

[29]Popov, G., Kim, V., Tikhonov, V., Semenikhin, S., and Tibrina, M., "The Fourth (Final) Quarterly Report on the Milestones," NASA JPL-960938, Dec. 1998.

[30]Choueiri, E. Y., and Okuda, H., "Anomalous Ionization in MPD Thrusters," 23rd International Electric Propulsion Conf., Paper IEPC-93-067, 1993.

[31]Heiermann, J., and Auweter-Kurtz, M., "Numerical and Experimental Investigation of the Current Distribution in Self-Field MPD Thrusters," AIAA Paper 2001-3498, 2001.

[32]Abramov, V. A., Dontsov, I. U. P., Kogan, V. I., Kovrov, P. E., Morozov, A. I., Vinogradova, A. K., and Zaveniagin, I. U. A., "Investigation of Electron Temperature and Plasma Radiation in a Quasi-Steady High-Current Discharge Between Coaxial Electrodes," *Proceedings of the 8th International Conference on Phenomena in Ionized Gases*, 1968.

[33]Sankaran, K., "Simulation of MPD Flows Using a Flux-Limited Numerical Method for the MHD Equations," M.S. Thesis, Princeton Univ., Princeton, NJ, 2001.

[34]Jahn, R. G., *Physics of Electric Propulsion*, McGraw–Hill, New York, 1968, Chap. 8, pp. 240–246.

[35]Choueiri, E. Y., "Scaling of Thrust in Self-Field MPD Thrusters," *Journal of Propulsion and Power*, Vol. 14, No. 5, 1998, pp. 744–753.

[36]Barnett, J. W., "Operation of the MPD Thruster with Stepped Current Input," Ph.D. Dissertation, Mechanical and Aerospace Engineering Dept., Princeton Univ., Princeton, NJ, 1985.

[37]Turchi, P. J., and Jahn, R. G., "Cathode Region of a Quasi-Steady MPD Arcjet," *AIAA Journal*, Vol. 9, No. 7, 1971, pp. 1372–1379.

[38]Kelly, A. J., and Jahn, R. G., "Pulsed Electromagnetic Acceleration: JPL Contract no.954997," Mechanical and Aerospace Engineering Dept., Princeton Univ., Rept. 1692.23, 1986.

[39]Boyle, M. J., "Acceleration Processes in the Quasi-Steady Magnetoplasmadynamic Discharge," Ph.D. Dissertation, Princeton Univ., Princeton, NJ, 1974.

[40]Turchi, P. J., "The Cathode Region of a Quasi-Steady Magnetoplasmadynamic Arcjet," Ph.D. Dissertation, Mechanical and Aerospace Engineering Dept., Princeton Univ., Princeton, NJ, 1970.

[41]DiCapua, M. S., "Mass, Momentum and Energy Flow from an MPD Accelerator," Ph.D. Dissertation, Mechanical and Aerospace Engineering Dept., Princeton Univ., Princeton, NJ, 1971.

[42]Jahn, R. G., von Jaskowsky, W. F., and Clark, K. E., "Pulsed Electromagnetic Acceleration," Mechanical and Aerospace Engineering Dept., Princeton Univ., Rept. 1467a, 1979.